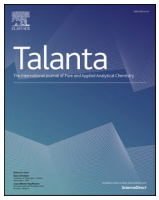
Talanta 291 (2025) 127873



Contents lists available at ScienceDirect

Talanta

journal homepage: www.elsevier.com/locate/talanta



CRISPR/Cas12a *trans*-cleavage cascading dual-template exponential amplification reaction for electrochemiluminescent detection of 17β-estradiol in milk

Hang Du, Yu-Yi Zhou, Jia-Wen Wu, Ye-Yu Wu, Jun Yan, Xue-Cai Tan *, De-Fen Feng **, Ke-Jing Huang ***

Education Department of Guangxi Zhuang Autonomous Region, Laboratory of Optic-electric Chemo/Biosensing and Molecular Recognition, Guangxi Collaborative Innovation Center for Chemistry and Engineering of Forest Products, Guangxi Key Laboratory of Chemistry and Engineering of Forest Products, Key Laboratory of Chemistry and Engineering of Forest Products, State Ethnic Affairs Commission, School of Chemistry and Chemical Engineering, Guangxi Minzu University, Nanning 530006, China

ARTICLE INFO

Keywords:
Metal-organic framework
CRISPR-Cas12a system
Dual-template exponential amplification
17β-estradiol

ABSTRACT

17β-Estradiol (E2) is a common environmental estrogen that can interfere with the endocrine systems of humans and animals, and poses a carcinogenic risk even at picomolar concentrations. In this study, a functionalized Ru(bpy)$_3^{2+}$-embedded metal-organic framework (ZnRuMOF) is synthesized, in which Ru(bpy)$_3^{2+}$ served as an electrochemiluminescence (ECL) indicator and the porous structure of ZnRuMOF acts as a nanoreactor to enhance the ECL signal. Based on this, we developed an E2 detection method combining a highly specific CRISPR-Cas12a system and dual-template exponential amplification. This method utilizes the *trans*-cleavage activity of CRISPR-Cas12a to control a light switch, achieving precise and ultra-sensitive detection of E2. The sensing platform demonstrates excellent performance in detecting E2 concentrations ranging from 1 fg mL^{-1} to 150 ng mL^{-1}, with a detection limit of 0.27 fg mL^{-1} (S/N = 3). This study provides a reliable approach for diagnosing and treating diseases related to E2, aiming to protect environmental quality and human health.

1. Introduction

17β-estradiol (E2) is an important sex hormone, widely present in the environment, and has a significant impact on the endocrine systems of humans and animals [1,2]. E2 interferes with endocrine activities, affect growth, metabolism and reproduction, and may even cause cancer [3]. The widespread presence of E2 in the environment has become an emerging public health issue, potentially threatening human health and aquatic organisms. This has increased the demand for E2 detection, especially concerning food safety and human health [4]. The main methods for detecting E2 in food are liquid chromatography-mass spectrometry and high-performance liquid chromatography (HPLC), which can accurately measure E2 levels [5,6]. However, these methods have the limitations of poor selectivity, low sensitivity, and slow detection speed. Therefore, developing an E2 detection method with high selectivity, sensitivity, and rapid response is of significant importance [7].

ECL is a method that combines chemiluminescence with electroanalytical techniques, offering excellent performance [8]. Its low detection limit can reach the picomolar level, with background noise as low as a few picoamperes, and a wide linear range, typically covering concentrations from 10^{-4} M to 10^{-12} M [9–11]. However, when analyzing small molecules (such as environmental hormones), ECL still faces some challenges. Particularly, when the sample contains complex matrix components and the analyte concentration is extremely low, matrix interference can occur, potentially affecting the accuracy of the final detection results.

One approach to enhance the sensitivity of ECL sensors is to incorporate nanomaterials, especially metal-organic frameworks (MOFs) and their metal ion clusters [12]. In recent years, MOFs have shown significant advantages in the field of electrochemical sensing [13]. MOFs have a large specific surface area, providing abundant active sites that

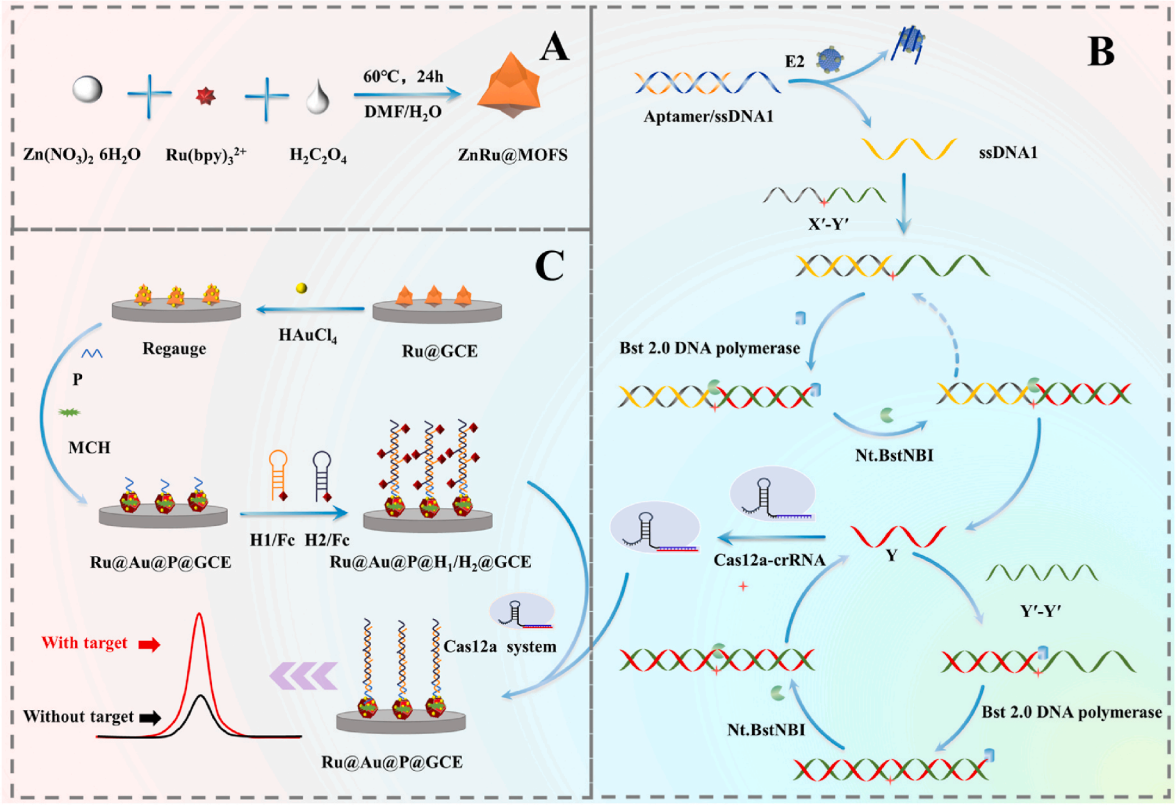
* Corresponding author.
** Corresponding author.
*** Corresponding author.
E-mail addresses: gxunxctan@126.com (X.-C. Tan), dffeng21@126.com (D.-F. Feng), kejinghuang@163.com (K.-J. Huang).

https://doi.org/10.1016/j.talanta.2025.127873
Received 5 January 2025; Received in revised form 12 February 2025; Accepted 1 March 2025
Available online 2 March 2025
0039-9140/© 2025 Elsevier B.V. All rights are reserved, including those for text and data mining, AI training, and similar technologies.

enhance sensor sensitivity [14,15]. By adjusting the metal and organic ligands, their pore size and chemical environment can be optimized to improve selectivity for specific analytes [16]. Incorporating $Ru(bpy)_3^{2+}$ into MOFs can significantly enhance its light absorption and catalytic activity. This photosensitizer exhibits high luminescence efficiency (quantum yield of 0.5–0.9) and excellent luminescent stability, making it suitable for ECL biosensing and environmental monitoring [17]. However, its high solubility in aqueous solutions and tendency to detach may affect the stability and sensitivity of sensors. Encapsulating $Ru(bpy)_3^{2+}$ within the pores of MOFs can improve its stability, prevent detachment, degradation, and side reactions, thereby enhancing the performance of ECL heterogenous detection [18–20]. This experiment employs a heterogeneous reaction mechanism, where free radicals are generated through the reaction of triethylamine (TEA), which then undergo further reaction with $Ru(bpy)_3^{2+}$ to form the excited state $Ru(bpy)_3^{2+}$*. Ultimately, orange light at 610 nm is emitted as the system relaxes from the excited state to the ground state [21].

In addition, by integrating nucleic acid signal amplification strategies into the ECL detection system, its specificity and sensitivity can be significantly enhanced [22]. In recent years, the CRISPR/Cas12a system has gained widespread attention for its ability to highly specifically cleave double-stranded DNA (*cis*-cleavage) and independently cleave single-stranded DNA (non-sequence-specific cleavage), making it widely used in genome editing and medical diagnostics, thus providing greater flexibility for the design of biosensors [23–25]. In recent years, various isothermal amplification methods have been developed for sensor signal amplification, among which the Exponential Amplification Reaction (EXPAR) uses specific primers and DNA polymerase to achieve exponential amplification of target nucleic acids under isothermal conditions, significantly improving sensitivity and efficiency (signal can be amplified up to millions of times) with a short reaction time (from a few minutes to tens of minutes) [26,27]. This technique is widely used in molecular detection and quantification. Integrating the CRISPR/Cas12a system into a new ECL platform is expected to further enhance its sensitivity and selectivity.

In this study, a luminescent ZnRuMOF is synthesized hydrothermally, and a dual-template exponential amplification reaction is combined with the CRISPR/Cas12a system to develop a new method for detecting E2. As shown in Scheme 1, ZnRuMOF is synthesized under hydrothermal conditions using oxalic acid as the ligand and zinc nitrate as the Zn^{2+} source (Scheme 1A). In Scheme 1B, we design a dual-amplified ECL strategy based on the CRISPR/Cas12a system and EXPAR for high-sensitivity detection of E2. Firstly, ssDNA (DNA1) hybridizes with the aptamer to form a stable double-stranded DNA structure (dsDNA), and then E2 opens the dsDNA structure and competitively replaces ssDNA. During the replacement process, ssDNA is first directed to the template X′-Y′ for amplification cycles and extends under the action of Bst 2.0 DNA polymerase to generate dsDNA with an upper-stranded cleavage enzyme recognition site. Subsequently, the specific amplification product Y is released by the endonuclease (Nt.BstNBI) cutting the nucleic acid chain X′-Y′, which is further bound to another template, Y′-Y′ to trigger a new double-stranded extension and release cycle, thereby generating a large number of Y. The Y then binds with crRNA, triggering nonspecific excision features in the CRISPR/Cas12a system. As shown in Scheme C, the ZnRuMOF modified on the surface of the glassy carbon electrode (GCE) produces a significant initial ECL intensity due to the large amount of $Ru(bpy)_3^{2+}$ loaded, and then AuNPs are electroplated and the chain ssDNA-P (P-DNA) is fixed to the electrode surface (ssDNA/AuNPs/ZnRuMOF) through gold-sulfur bonds, resulting in a gradual weakening of the ECL signal. Ferrocene (Fc) is introduced to the electrode surface through hybridization chain reactions (HCR) and reacts with $Ru(bpy)_3^{2+}$, resulting in a significant weakening of ECL intensity. Finally, on the modified GCE surface, the Fc-linked ssDNA is cleaved through the CRISPR/Cas12a system, and the ECL intensity is restored.



Scheme 1. (A) Diagram illustrating the synthesis process of ZnRuMOF material; (B) Dual template exponential amplification reactions and activation of the CRISPR-Cas12a System; (C) ECL detection of E2 with the modified electrode.

2. Experimental section

2.1. Reagents and instrumentation

For detailed information on the experimental instruments and reagents, please refer to the supporting information.

2.2. Preparation of ZnRuMOF materials

ZnRuMOF was prepared according to a previous report [28]. Two hundred microliters of oxalic acid (0.75 M) and 3 mL of hydrochloric acid (1 M) were combined in 45 mL of a 2:1 (V/V) DMF and water mixture. Then, 15 mg of $Ru(bpy)_3Cl_2{\cdot}6H_2O$ and 100 mg of $Zn(NO_3)_2$ were added to the mixture. After a 5-min sonication, the mixture was refluxed at 60 °C for 24 h. An orange-red precipitate was collected after copious sequential washing with DMF, ethanol, and ultrapure water, followed by an overnight vacuum drying at 50 °C.

2.3. Preparation of DNA products

The aptamer strand was complexed with the DNA single strand to form a ds-structure through base complementary pairing. When the target molecule E2 was present, its strong specific binding capability facilitated the release of the ssDNA single strand. Two distinct 20 μL EXPAR reaction mixtures, A and B, were prepared. Mixture A consisted of 10 μL of a desired concentration of ssDNA, 2 μL template strand-X′-Y' (5 μM), 2 μL template strand-Y′-Y' (2.5 μM), and 6 μL dNTP (500 μM). Mixture B consisted of 10 μL of 0.4 U/μL Nt.BstNBI [2 μL buffer + 2 μL cut-off nucleic acid endonuclease + 6 μL enzyme-free water] and 1 μL NEBuffer™, 1 μL Bst 2.0 DNA polymerase (0.08 U/μL) and 8 μL isothermal amplification buffe. After thoroughly mixing A and B, the ssDNA released was added dropwise to the mixture and incubated at 55 °C for 2 h to obtain the amplified product Y strand. Then, 10 μL of Y-strand was mixed with 5 μL of 100 nM crRNA and 5 μL of 100 nM Cas12a. The mixture was then incubated together at 25 °C for 30 min.

2.4. Preparation of ECL biosensing platform

Firstly, a GCE was polished using 1.0 μm Al_2O_3 powder. The electrode were ultrasonically cleaned using ethanol and distilled water, respectively, followed by a stream of nitrogen. Then, 9 μL aliquots of a 0.5 mg mL^{-1} ZnRuMOF solution was applied to the electrode surface and was allowed it to dry naturally at room temperature. Subsequently, CV was employed to uniformly deposit a 1 mg mL^{-1} $HAuCl_4$ solution onto the electrode surface. The experimental scanning range was set from −1 V to 1.15 V, with a scanning rate of 0.1 mV s^{-1}, and two scanning cycles were conducted. Then, 6 μL of 4 μM ssDNA with sulfhydryl groups was added on the electrode and kept at 37 °C for 4 h. Next, 10 μL of 1 mM MCH solution was added and incubated for 30 min to block the active sites. Subsequently, excess DNA strand was washed off with phosphate buffered saline (PBS) (0.1 M, pH 7.4). Subsequently, the Fc-labeled DNA strands were uniformly coated onto the electrode and enriched at 37 °C for 80 min to promote HCR. Finally, the activated Cas12a protein was added to the electrode for an 80 min reaction, effectively cleaving the Fc-DNA single strands modified on the HCR framework, thereby restoring the luminescence.

2.5. Pretreatment of real-life real samples

The milk used in this study was purchased from a school supermarket. In our work, 1 mL of E2 standard solution of increasing concentration from 0.0003 to 1500.0 ng mL^{-1} ng·mL^{-1} was added to 2 mL of the sample, followed by mixing with 7 mL of ethanol, before being centrifugation at 10000 rpm for 10 min. Subsequently, 1 mL of the supernatant was filtered through a 0.45 μm membrane, and then diluted with 0.01 M PBS (pH 7.4) to a total volume of 10 mL.

2.6. Chromatography conditions setting

For chromatography detection, an Agilent eclipse C18 chromatography column was used. The column temperature was maintained at 30 °C. The injection volume was 10 μL. Mobile phase A was a 60 % methanol solution, and mobile phase B was 40 % water, with a flow rate of 1.0 ml min^{-1}. The wavelength for quantitative detection was 280 nm.

2.7. Sensor assembly and testing

The detailed data on sensor assembly and testing, please refer to the supporting information.

3. Results and discussion

3.1. Characterization of nanomaterials

The structure of the ZnRuMOF material is analyzed using SEM and TEM. The micrographs in Fig. 1A to C present the ZnRuMOF material as small star-like polyhedral, where the micrograph in Fig. 1B is magnified 6.7 times that of Fig. 1A. The energy dispersive spectroscopy analysis results presented in Fig. S1 indicate that the composition of Zn is 18.15 % and that of Ru is 9.97 %. This suggests that the nanomaterials are primarily composed of Zn and Ru elements, with an atomic ratio close to 2:1. In addition, Fig. 1D reveals the distribution of Zn, Ru, C, and O within the MOF material. The results indicate a uniform distribution of these elements, further confirming the successful synthesis of the ZnRuMOF material. The presence of Ru can be accounted for by the uniform distribution of $Ru(bpy)_3^{2+}$ within the framework structure. We have used these results to infer a successful synthesis of the ZnRuMOF material.

Fig. 1E illustrates the FTIR sprays of $Ru(bpy)_3^{2+}$ (black), $H_2C_2O_4$ (blue) and ZnRuMOF (red) that illustrate two notable changes after $Ru(bpy)_3^{2+}$ is encapsulated in the MOF skeleton. In the infrared spectrum of ZnRuMOF, the disappearance of the characteristic carbonyl peak of carboxylic acids (1712 cm^{-1}) and the hydroxyl peak (around 3394 cm^{-1}), as the characteristic peak of free COO^- induced by $H_2C_2O_4$ diminished, it indicated the consumption of COO^- in the synthesis of ZnRuMOF. This phenomenon can be regarded as a direct result of the formation of the ZnRuMOF structure. Moreover, the prominent absorption bands observed in the range of 1752-1482 cm^{-1} may arise from the vibrations of the carboxyl groups in $H_2C_2O_4$, and they may also be associated with the stretching vibrations of the C═C double bonds in $Ru(bpy)_3^{2+}$. To further confirm the successful incorporation of Ru into the MOF, we conduct X-ray diffraction and the results are shown in Fig. S2. The results indicate that the positions of the diffraction peaks and the crystallinity of the samples remain similar before and after the incorporation of $Ru(bpy)_3^{2+}$. A series of diffraction peaks are observed at 12.8°, 14.1°, 18.7°, 20.8°, 22.6°, 23.1° and 30.2°, corresponding to the (102), (103), (004), (104), (210), (203) and (205) crystal planes. This demonstrates that the structural integrity of the MOF framework is maintained, and the introduction of $Ru(bpy)_3^{2+}$ did not significantly affect its original morphology.

Chemical composition and electronic valence states of the materials are also analyzed by X-ray photoelectron spectroscopy (XPS). As illustrated in Fig. 1F, the survey spectrum of ZnRuMOF shows the presence of Zn, Ru, O, and C. Fig. 1G indicates two distinct peaks at 1043.7 eV and 1021.0 eV, consistent with the $2p_{1/2}$ and $2p_{3/2}$ orbitals of zinc. At the same time, the Ru 3p spectrum in Fig. 1H show peaks at 461.7 eV, which corresponds to a Ru $3p_{3/2}$ orbital. In the Ru 3d spectrum in Fig. 1I, the two distinct peaks located at 279.8 eV and 284.0 eV are corresponding to the Ru $3d_{5/2}$ and $3d_{3/2}$ orbitals, respectively. These features demonstrate the fact that $Ru(bpy)_3^{2+}$ is successfully encapsulated in a MOF construct. Additionally, fluorescence testing of the material (Fig. 1J) reveals that under excitation at 480 nm, both $Ru(bpy)_3^{2+}$ and ZnRuMOF exhibit a broad emission peak centered at 625 nm, indicating that there is a strong

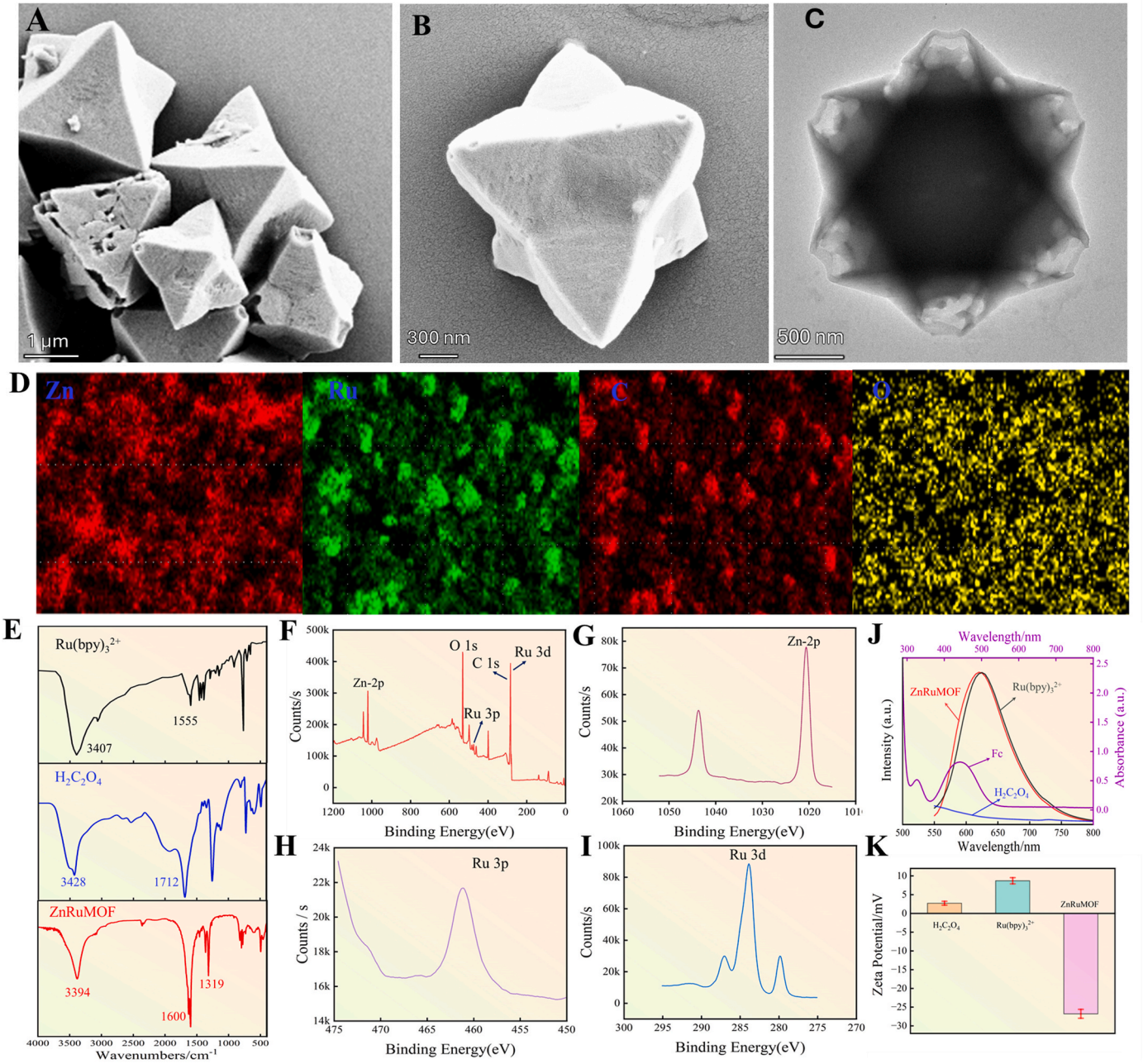


Fig. 1. Scanning electron microscopy (A, B) and transmission electron microscopy (C) of ZnRuMOF spectra (D) of (from left to right) the Zn, Ru, C, and O elements micrograph in ZnRuMOF. FTIR spectra (E) of $Ru(bpy)_3^{2+}$ (black) and $H_2C_2O_4$ (blue) ZnRuMOF (red). Survey X-ray photoelectron spectrum of ZnRuMOF (F); high-resolution X-ray photoelectron spectra of Zn 2p (G), Ru 3d (H) and Ru 3p (I). Ru 3p region and other elements of ZnRuMOF are analyzed using XPS, (J) Fluorescence spectra of $Ru(bpy)_3^{2+}$, $H_2C_2O_4$ and ZnRuMOF Fig. (K) The zeta potential of the $Ru(bpy)_3^{2+}$, $H_2C_2O_4$ and ZnRuMOF.

interaction between the two, which further confirmed the successful integration of $Ru(bpy)_3^{2+}$ with the MOF. Under room temperature conditions, we conducted systematic measurements of the zeta potential of $H_2C_2O_4$, $Ru(bpy)_3Cl_2{\cdot}6H_2O$ and ZnRuMOF and the results are shown in Fig. 1K. In these experiments, the pH of 5 mg mL^{-1} of each aqueous sample is adjusted to 7.0. Under the influence of an applied electric field of 100 V m^{-1}, the migration velocity of the charged particles is accurately determined by laser scattering, which is then used to evaluate the zeta potential (−20.88 V m^{-1} based on the Smoluchowski equation, $\zeta = \eta U/\varepsilon_r\varepsilon_o$, denotes viscosity of solvent, U the electrical mobility (obtained from the migration velocity and the electric field strength), the specific dielectric constant of solvent the dielectric constant in vacuum (8.854×10^{-12} C V^{-1} m^{-1}) [29,30]. To ensure the reliability of the results, each sample is measured at least three times. Among them, ZnRuMOF exhibits the highest zeta potential, suggesting a significant electrostatic adsorption capacity along with excellent dispersion and stability.

3.2. ECL performance and mechanism study

Fig. 2 shows the ECL responses of different electrodes. As indicated in Fig. 2A, the GCE does not exhibit any ECL in the presence of TEA (curve a). In contrast, after immobilizing ZnRuMOF on the GCE surface, the luminescent agent $Ru(bpy)_3^{2+}$ produces an ECL response of 12,066 in the presence of TEA, as shown by curve b. When Fc is modified onto the electrode through HCR, the ECL response is suppressed. This is primarily due to the formation of Fc* upon energy absorption, which can react

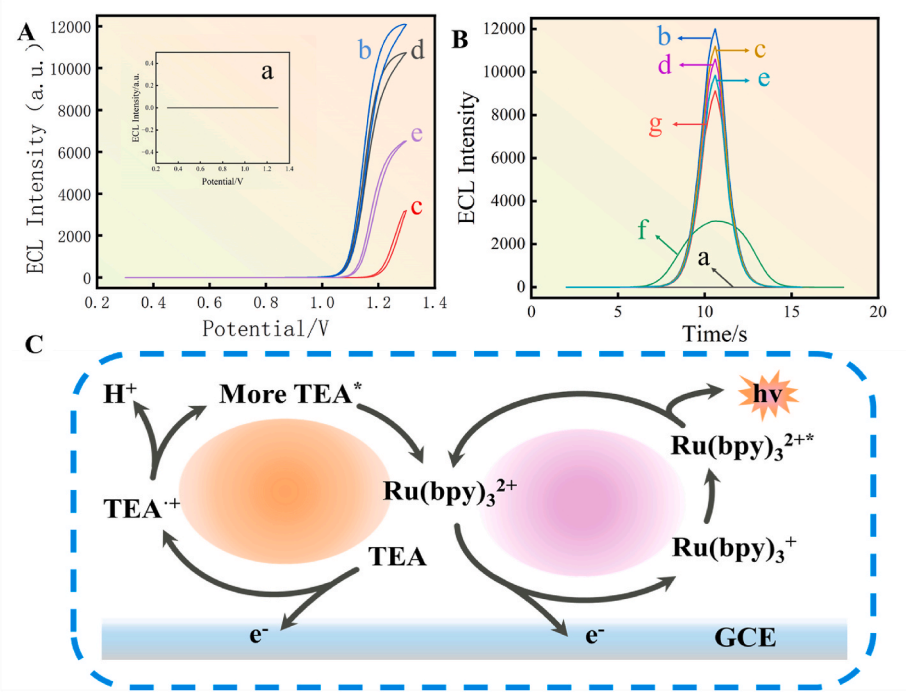


Fig. 2. (A) ECL intensity versus potential plot at bare GCE (a), ZnRuMOF/GCE (b), H1-Fc + H2-Fc/ZnRuMOF/GCE (c), Cas12a-crRNA (Dual-template exponential amplification reaction)/H1+H2/ZnRuMOF/GCE (d), Cas12a-crRNA (Single-template exponential amplification reaction)/H1+H2/ZnRuMOF/GCE (e)in 0.1 M PBS containing 20 mM TEA (pH 7.4); (B) ECL intensity time plots of bare GCE (a), ZnRuMOF/GCE (b), AuNPs/ZnRuMOF/GCE (c), ssDNA/AuNPs/ZnRuMOF/GCE (d), MCH/ssDNA/AuNPs/ZnRuMOF/GCE (e), H1-Fc + H2-Fc/MCH/ssDNA/AuNPs/ZnRuMOF/GCE (f), and Cas12a-crRNA/H1+H2/MCH/ssDNA/AuNPs/ZnRuMOF/GCE (g) in 0.1 M PBS containing 20 mM TEA (pH 7.4); (C) A schematic diagram of the ECL mechanism. The reaction medium is 0.1 M PBS containing 20 mM TEA (pH 7.4).

with the excited state of $Ru(bpy)_3^{2+}$* (curve c). When the Cas12a protein activated by the double-template exponential amplification reaction is added to the Fc-modified GCE surface, Cas12a cleaves the Fc-labeled DNA strand, causing the DNA strand to detach from the electrode and significantly restoring the ECL signal (curve d). However, when the Cas12a protein activated by the single-template exponential amplification reaction is added to the same electrode surface, the ECL signal can only be restored to 7000 (curve e), indicating that the double-template exponential amplification reaction is more effective than the single-template reaction in enhancing Cas12a activity and ECL response.

Fig. 2B shows the ECL response at each step of the preparation process of the sensing platform in 0.1 M PBS containing 20 mM TEA (pH 7.4). The GCE does not exhibited any obvious ECL response (curve a). After the electrode modification with ZnRuMOF, the ECL intensity significantly increases to 12011 a.u. (curve b). However, with the successive addition of AuNP, ssDNA, and MCH, the ECL response of the electrode decreases by 11203 a.u. (curve c), 10605 a.u. (curve d), and 9941 a.u. (curve e), respectively. Further modification of the Fc-functionalized electrode through HCR, the ECL intensity significantly decreases to 2934 a.u. (curve f). This can be attributed to the interaction between ferrocene and $Ru(bpy)_3^{2+}$, which severely hinders the electron transfer process. When activated Cas12a-crRNA is incubated with H1-Fc + H2-Fc/MCH/ssDNA/AuNPs/ZnRuMOF/GCE, it can cleave DNA single strands with Fc groups, thereby restoring the ECL response to a certain extent to 9582 a.u. (curve g). In addition, the DNA backbone generated by the HCR also hinders electron transfer, resulting in further attenuation of the ECL signal from ZnRuMOF. Overall, these results validate the successful construction of the sensor platform.

As shown in Fig. 2C, due to its good conductivity, ZnRuMOF mediates the injection of a large number of electrons, which leads to an increase in the half-life of the $TEA^{\cdot+}$, causing it to shed more protons on the α-carbon, resulting in the generation of the highly reducing intermediate TEA·. A large number of radicals can transfer electrons to the π* orbitals of $Ru(bpy)_3^{2+}$, thus promoting the reduction of $Ru(bpy)_3^{3+}$ to $Ru(bpy)_3^{2+}$. When $Ru(bpy)_3^{2+}$* returns to its ground state, it emits energy as an optical signal. The specific luminescence mechanism of $Ru(bpy)_3^{2+}$ in the presence of TEA as a co-reactant can be described by the following equations [31]:

$$TEA\text{-}e \rightarrow TEA^{\cdot+}$$

$$TEA^{\cdot+}\text{-}H^{+} \rightarrow TEA^{*}$$

$$TEA^{*} + Ru(bpy)_3^{2+} \rightarrow Ru(bpy)_3^{+} + product$$

$$Ru(bpy)_3^{+} + TEA^{\cdot+} \rightarrow Ru(bpy)_3^{2+*} + product$$

$$Ru(bpy)_3^{2+*} \rightarrow Ru(bpy)_3^{2+} + hv$$

3.3. Electrochemical characterization and feasibility study

Electrochemical impedance spectroscopy of 0.1 M $[Fe(CN)_6]^{3-}$ is conducted at a GCE in 1 ng mL^{-1} E2 as a supporting electrolyte to monitor changes in the modified electrode surface during each assembly step. The results obtained are shown in Fig. 3A. The AC impedance spectrum of $[Fe(CN)_6]^{3-}$ at the bare GCE shows a small semicircle in the high frequency region and a linear impedance in the low frequency region. By estimating the charge transfer resistance (*Rct*) by the diameter of the semicircle, this is measured directly from curve a in Fig. 3A to be 2.64 Ω. After modification with the ZnRuMOF material, the resistance value significantly increases to 26.33 Ω, as shown in curve b. This phenomenon can be attributed to the uneven contact or poor contact quality between ZnRuMOF and the electrode surface, which hinders charge transfer and subsequently increases the interfacial resistance. After depositing AuNPs on the electrode used in curve c, *Rct* is reduced to 11.76 Ω, owing to the enhanced conductivity. This is mainly

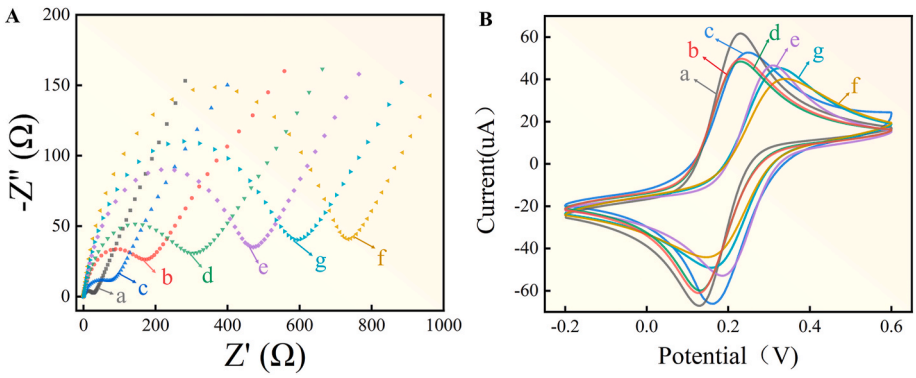


Fig. 3. Assessing step-by-step fabrication of EIS (A) and CV (B) for biosensors:(a) Bare electrodes, (b) ZnRuMOF/GCE, (c) AuNPs/ZnRuMOF/GCE, (d) ssDNA/AuNPs/ZnRuMOF/GCE, (e) MCH/ssDNA/AuNPs/ZnRuMOF/GCE, (f) H1-Fc + H2-Fc/MCH/ssDNA/AuNPs/ZnRuMOF/GCE, (g) Cas12a-crRNA/H1+H2/MCH/ssDNA/AuNPs/ZnRuMOF/GCE.

attributed to the excellent conductivity of the AuNPs, which allows for more efficient electron conduction, thereby enhancing the overall conductivity and ultimately reducing the resistance. After modifying a AuNP/ZnRuMOF/GCE with an ssDNA, *Rct* increases to 30.90 Ω in curve d. This is due to the long-chain structure of the DNA, which generates a noticeable spatial hindrance on the electrode surface, restricting the migration of electrons and ions, thereby increasing the resistance to the charge transfer process. In addition, the self-assembled monolayer forms on the electrode surface after MCH modification occupies nonspecific sites, causing spatial hindrance that restricted the migration of electrons and ions. This effect further leads to a significant increase in the R_{ct}, reaching 35.08 Ω (curve e). After modifying the electrode with hairpin H1 and hairpin H2 (curve f), the R_{ct} of the electrode significantly increases to 41.24 Ω. This phenomenon is attributed to the larger volume of the ferrocene groups, leading to spatial hindrance on the electrode surface, thereby restricting the migration of electrons and ions. Finally, when the activated Cas12a protein is added to the electrode (curve g), the R_{ct} value decreases to 40.23 Ω. This phenomenon can be attributed to the cleavage of the Fc groups from hairpin H1 and H2 by the Cas12a protein. The removal of the Fc groups reduces the spatial hindrance on the electrode surface, allowing electrons and ions to migrate more freely, thereby effectively lowering the charge transfer resistance.

Cyclic voltammetry of 1 ng mL^{-1} E2 in 0.1 M $K_3[Fe(CN)_6]/K_4[Fe(CN)_6]$ as a supporting electrolyte is performed to characterize every step of the sensor fabrication procedure, and the results obtained are displayed in Fig. 3B. Curve a shows a $[Fe(CN)_6]^{3-}$ oxidation peak of 72.04 μA at 0.23 V, and a reduction peak of 72.20 μA at 0.13 V at the bare GCE. Due to the introduction of greater interfacial impedance between the electrode and the electrolyte by the ZnRuMOF composite material, electron transfer is inhibited. As a result, the oxidation peak current of the ZnRuMOF-modified GCE decreases to 56.10 μA, and the reduction peak current is 61.81 μA (curve b), which represents a decrease of 15.94 μA in the oxidation peak current and an increase of 10.39 μA in the reduction peak current compared to the bare GCE. After further gold deposition treatment, the oxidation peak current increases to 58.81 μA, while the reduction peak current is 62.23 μA (curve c). Compared to the GCE modified with ZnRu MOF materials, the oxidation peak current rises by 2.71 μA and the reduction peak current increases by 0.42 μA. This change is attributed to the superior conductivity of AuNPs, which significantly enhances the rate of electron transfer. After the modification of the DNA single strand on the Au NPs/ZnRuMOF/GCE, the oxidation peak current is observed to be 55.47 μA, while the reduction peak current is 61.61 μA (Curve d). This phenomenon is attributed to the electrostatic repulsion between the DNA and the ferrocyanide probe. When MCH is used to block the active sites, a self-assembled monolayer forms on the electrode surface. This layer significantly hinders the free approach of reactants, thereby affecting their concentration and reaction rate, ultimately leading to a positive shift in the CV peaks. Moreover, this film interferes with the electron transfer processes at the electrode surface, resulting in a decrease in current. Additionally, the oxidation peak current decreases to 54.94 μA, while the peak current increases to 53.18 μA (curve e). After applying the H1 and H2 hairpin modifications on the GCE, the current values decrease significantly, with the oxidation peak current dropping to 38.16 μA and the reduction peak current rising to 38.24 μA. This phenomenon is attributed to the increased electrostatic repulsion between deoxyribonucleic acid and the potassium ferricyanide probe (curve f). Finally, after the activated Cas12a protein modified the GCE, the deoxyribonucleic acid undergoes significant separation, mitigating the electrostatic repulsion with the potassium ferricyanide probe. This makes an increase of the oxidation peak current to 47.16 μA, while the reduction peak current decreases to 45.77 μA (curve g). These characterizations further confirm the successful assembly of the sensor.

3.4. *Optimization of experimental conditions*

The experimental conditions play a crucial role in the analytical performance. To achieve the best biosensor performance, three main parameters affecting the assay performance are optimized, such as the amount of ZnRuMOF material, the concentration of Nt.BstNBI enzyme, the concentration of Bst 2.0 DNA polymerase, amplification reaction time, HCR reaction time, and Cas12a reverse cutting time. As shown in Fig. 4A, as the amount of ZnRuMOF material modified on the GCE surface increases, the ECL intensity gradually enhances. The highest intensity of ECL response is obtained when the amount of ZnRuMOF material increases to 9 μL. This is because the limited surface area of GCE cannot accommodate additional composite material effectively, and a thick ECL-sensitive membrane is detrimental to detection efficiency. Therefore, further increasing the dosage does not enhance ECL intensity. As a result, it is found that 9 μL of ZnRuMOF material is ideal for subsequent measurements. Fig. 4B illustrates the effect of Nt.BstNBI enzyme concentration ranging from 0.1 U/μL to 0.6 U/μL. As the enzyme concentration increases, there is a noticeable increase in ECL intensity. However, higher enzyme concentrations may trigger side reactions, leading to increased background noise and experimental errors. Considering the overall experimental performance, a concentration of 0.4 U/μL was selected as the optimal enzyme concentration. Fig. 4C illustrates the effect of Bst 2.0 DNA polymerase concentration ranging from 0.04 U/μL to 0.2 U/μL on the reaction. Excessively high enzyme concentrations may lead to the rapid depletion of substrates (such as dNTPs) during the early stages of amplification, resulting in substrate scarcity, which in turn affects the continuity and efficiency of the reaction. After considering the stability and performance of the reaction, a concentration of 0.08 U/μL was selected as the optimal enzyme

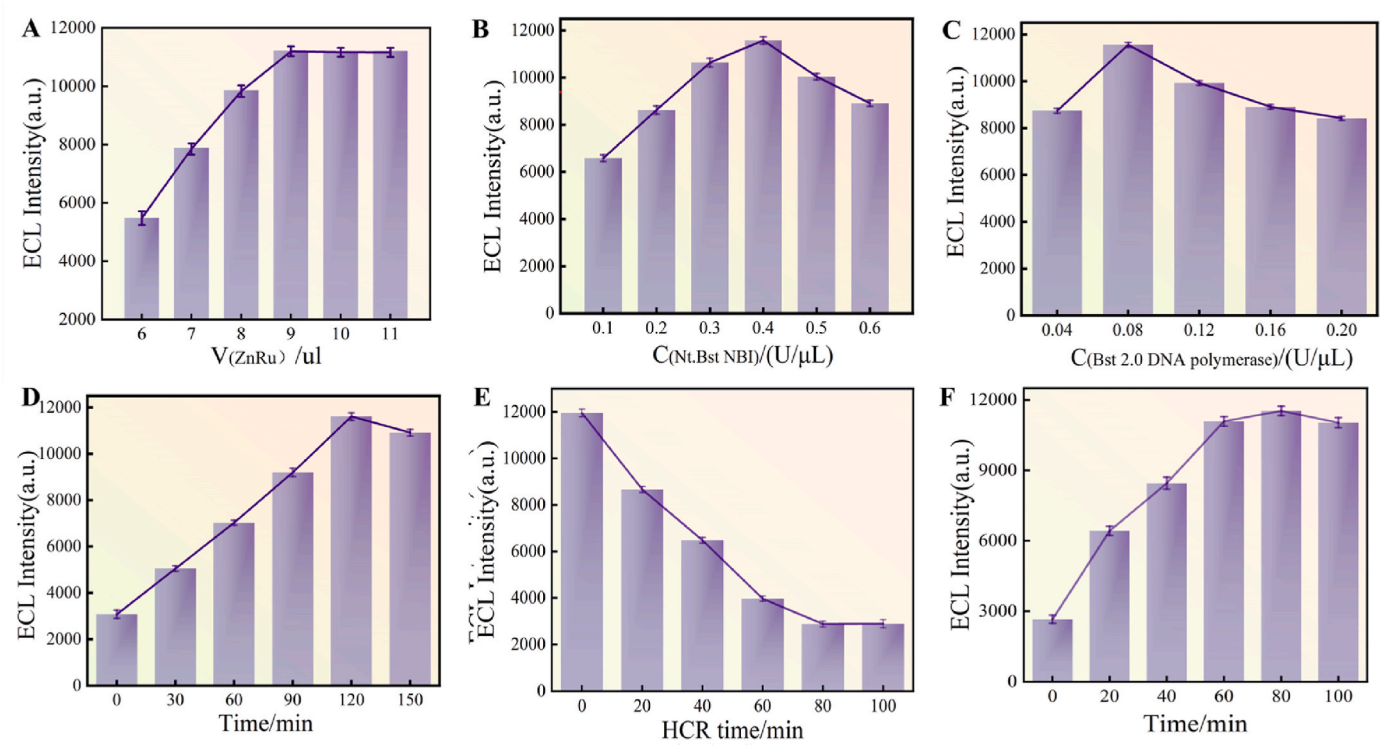


Fig. 4. The effect of amount of ZnRuMOF material (A), concentration of Nt.BstNBI enzyme (B), concentration of Bst 2.0 DNA polymerase (C), amplification reaction time (D), HCR time of hairpin H1 and H2 (E) and Cas12a trans cutting time (F).

concentration. Fig. 4D shows the effect of amplification reaction time, ranging from 30 min to 150 min, on the ECL signal. The results indicate that the ECL signal peaked at 120 min, after which the signal began to decrease. This decline may be due to the prolonged reaction time causing a gradual reduction in enzyme activity, which in turn affects the reaction efficiency. Therefore, 120 min was determined as the optimal reaction time for the exponential amplification. As shown in Fig. 4E, the HCR is performed by hairpin H1-Fc and hairpin H2-Fc after base

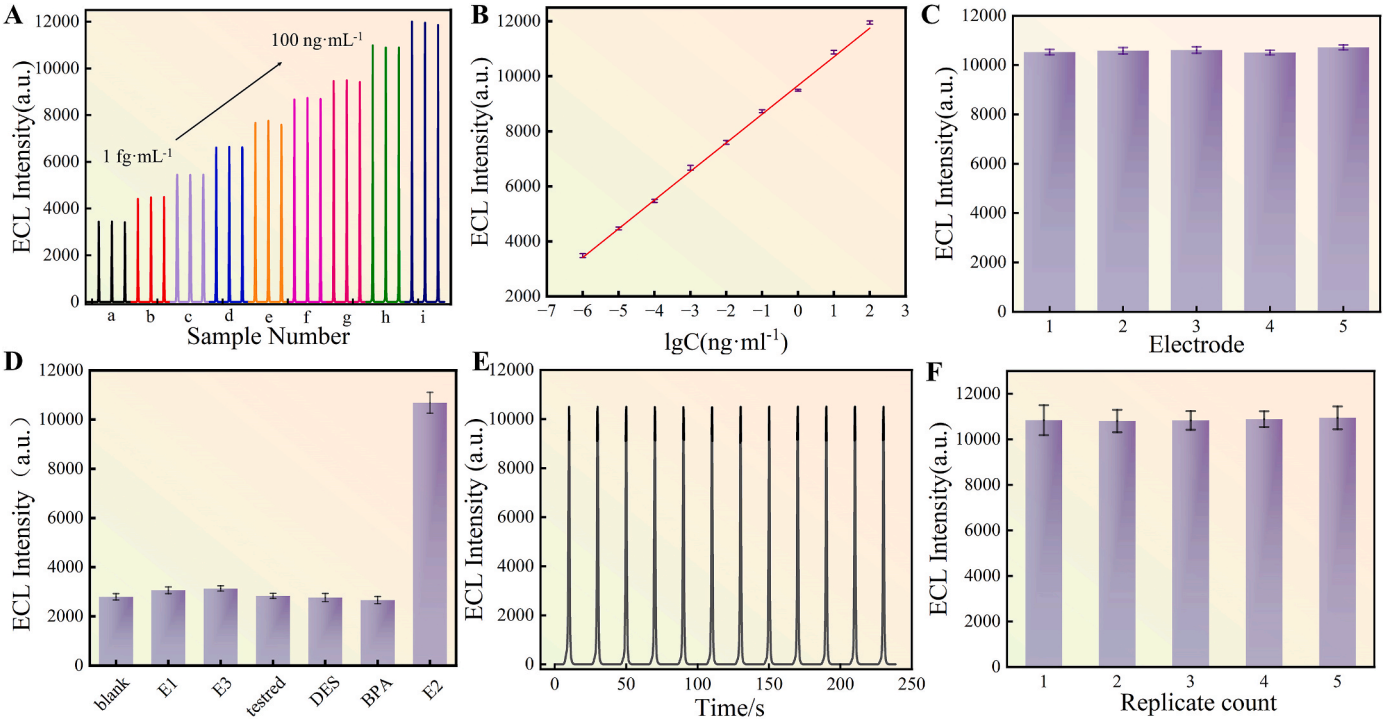


Fig. 5. (A) ECL response at different concentrations of E2 (a–i: 10^{-6}, 10^{-5}, 10^{-4}, 10^{-3}, 10^{-2}, 10^{-1}, 1, 10, and 10^{2} ng mL^{-1}); (B) Logarithmic relationship between E2 concentrations and ECL intensity; (C) Repeatability of the proposed biosensor; (D) Selectivity of biosensors for different substances. (E) The stability of the biosensor. (F) Testing with different electrodes at the same concentration.

complementary pairing to form ssDNA modified on P-DNA/AuNPs/ZnRuMOF/GCE. The ECL intensity tends to decrease in the reaction time range of 20–100 min. The results show that the best inhibition of luminescence is achieved when the reaction time is 80 min, and the luminescence intensity remains unchanged when the time is further extended. Fig. 4F shows the effect of Cas12a reverse cutting time. As the reaction time extends from 20 min to 60 min, there is an increasing trend in ECL intensity. With increasing reaction time, the ECL intensity increases. Considering detection efficiency, 80 min is selected as the optimal incubation time to enhance detection efficiency. In this study, when conducting optimization experiments using the traditional one-variable-at-a-time approach, we did not consider any potential interactions between parameters.

3.5. Analytical performance

The ECL sensing platform is employed to detect varying concentrations of E2 under optimal experimental conditions, with five parallel samples conducted for each concentration to calculate the average value. In Fig. 5A, as the E2 concentration increases from 1 fg mL^{-1} from 100 ng mL^{-1}, the intensity of the ECL response gradually increases. By plotting the ECL response in Fig. 5A against lgC_{E2}, shown in Fig. 5B, the coefficient of determination (R^2) reached 0.997, indicating a significant linear correlation. The regression equation derived from fitting is $Y = 1041.5\ lgC + 9667.6$. Based on a calculation of 3 times the standard deviation (3σ), the detection is estimated to be 0.27 fg mL^{-1}.

The comparison with other E2 sensors is detailed in Table 1. Our method significantly improves the efficiency and signal amplification capability of the sensor, effectively lowers its detection limit, and broadens its linear measurement range. The reproducibility of this ECL method is validated by testing five electrodes prepared under identical conditions for the detection of E2 at 1 ng mL^{-1}. As shown in Fig. 5C, the ECL sensing platform exhibits acceptable reproducibility with a relative standard deviation (RSD) of 0.7 %. Selectivity is crucial for validating an analysis, and we selected five potential interferents: estrone (E1), estriol (E3), testosterone (testred), hexestrol (DES), and bisphenol A (BPA). Fig. 5D shows that the change in ECL response signal intensity between the control and intervention groups is negligible, indicating that the sensing platform has good anti-interference ability. Moreover, at lower concentrations of the substance (Fig. S5), the biosensor still demonstrates significant selectivity for E2, further confirming its excellent recognition performance. Fig. 5E demonstrates the ECL response for 1 ng mL^{-1} E2 over 12 consecutive cycles on a single sample, with an RSD of 0.25 %, indicating significant stability. The ECL intensity remains stable with no significant variation, and using different electrodes to detect the same concentration yields relatively stable ECL response values. These results confirm that the biosensor possesses excellent selectivity, reproducibility, and stability, making it suitable for complex, real-life samples.

Table 1
Comparison with other sensors for E2 detection.

Measurement technique	Combination method	Linear range	LOD	Ref
ECL	E2-Monoclonal antibody	0.1 pg·mL^{-1}-0.2 pg mL^{-1}	10.0 fg mL^{-1}	[32]
ECL	E2- Aptamer	0.01 pg·mL^{-1}-0.01 ng mL^{-1}	3.0 fg mL^{-1}	[33]
PEC	E2-Antibody	0.5 pg·mL^{-1}-20 ng mL^{-1}	300 fg mL^{-1}	[34]
ECL	E2-Antigen	0.1 pg·mL^{-1}-30 ng mL^{-1}	2.51 fg mL^{-1}	[35]
Fluorescent	E2- Aptamer	0.4 pg·mL^{-1}- 0.8 ng mL^{-1}	370 fg mL^{-1}	[36]
LICA	E2- Aptamer	7.2 pg mL^{-1} - 13 ng mL^{-1}	0.02 ng mL^{-1}	[37]
PEC	E2-Antibody	13.6 pg·mL^{-1}-0.23 ng mL^{-1}	268 fg mL^{-1}	[38]
ECL	E2- Aptamer	1.0 fg mL^{-1}-150 ng mL^{-1}	0.27 fg mL^{-1}	This work

3.6. Real-life sample analysis

The applicability of this ECL biosensor is assessed using the standard addition method. Prior to detection, all samples are pre-treated as described in Section 2.5. Different concentrations of E2 are added to the three types of milk samples, and then the constructed ECL platform is used for five separate detections, with the average value taken to obtain the response signal. The results, presented in Table 2, demonstrated the recoveries ranging from 90.0 % to 101.4 %.

Table S2 indicates that the ECL method achieves a recovery rate of 97.3 %–101.0 % for spiked samples, with a low relative standard deviation (RSD) between 1.1 % and 3.6 %. To further assess the performance of our developed biosensor, we utilized HPLC. HPLC analysis of various E2 concentrations demonstrated excellent separation in both standard and spiked blank sample chromatograms (Fig. S5 A-G). The standard calibration curve presented in Fig. S5 H shows recovery rates consistently between 98.6 % and 101.2 %, confirming HPLC's reliability in milk sample analysis. The high consistency between results from both ECL and HPLC methods for detecting E2 levels in real samples underscores their exceptional accuracy. The proposed ECL method holds significant potential for the effective detection of E2 in milk.

4. Conclusion

This study prepares ZnRuMOF materials encapsulating $Ru(bpy)_3^{2+}$ and develops a method for ultrasensitive detection of E2 based on the quenching of the ECL signal of $Ru(bpy)_3^{2+}$ by ferrocene. This method employs a cascade isothermal amplification strategy with the CRISPR/Cas12a system. By combining the CRISPR-Cas12a system with the traditional EXPAR method, the new approach effectively minimizes interference signals from non-specific amplification in EXPAR, with a slope of 1041.5, significantly enhancing the sensitivity and specificity of the method. The ECL biosensing platform exhibits exceptional performance, featuring a low detection limit for E2, a wide detection range, a low detection limit of 0.27 fg mL^{-1} (S/N = 3), and a broad linear range

Table 2
The results of standard addition method for real-life samples ($n = 3$).

Samples	E2 Concentration (ng·mL^{-1})		ECL Intensity	Recovery (%)	RSD (%)
	Added	Found			
Fresh milk	/	3.16×10^{-7}	2896.7	/	3.3
	3.0×10^{-5}	2.87×10^{-5}	4937.0	95.7	2.1
	2.0×10^{-3}	1.90×10^{-3}	6830.7	99.6	2.6
	1.0×10^{-1}	0.98×10^{-1}	8577.0	98.4	1.7
Low-fat milk	/	4.71×10^{-7}	3078.4	/	2.3
	3.0×10^{-5}	2.70×10^{-5}	4909.4	90.0	2.8
	2.0×10^{-3}	1.89×10^{-3}	6831.0	94.4	1.1
	1.0×10^{-1}	0.97×10^{-1}	8612.3	97.4	2.5
Breakfast milk	/	4.96×10^{-7}	3102.3	/	2.1
	3.0×10^{-5}	3.02×10^{-5}	4960.0	100.7	3.0
	2.0×10^{-3}	1.99×10^{-3}	6854.4	99.4	2.6
	1.0×10^{-1}	1.01×10^{-1}	8630.6	101.4	2.0

from 1 fg mL^{-1} to 150 ng mL^{-1} for E2. Moreover, the method demonstrates excellent reproducibility and stability, and has strong practicality. This study not only broadens the application scope of CRISPR/Cas12a but also provides a new and reliable option for the sensitive and accurate analysis of environmental hormones at ultra-low levels.

CRediT authorship contribution statement

Hang Du: Writing – original draft. **Yu-Yi Zhou:** Formal analysis, Conceptualization. **Jia-Wen Wu:** Methodology, Investigation. **Ye-Yu Wu:** Writing – review & editing, Methodology. **Jun Yan:** Writing – review & editing, Methodology. **Xue-Cai Tan:** Writing – review & editing, Supervision, Project administration, Methodology, Formal analysis, Conceptualization. **De-Fen Feng:** Writing – review & editing, Funding acquisition. **Ke-Jing Huang:** Writing – review & editing, Supervision, Methodology, Conceptualization.

Notes

The authors declare no competing financial interest.

Declaration of competing interest

The authors declared that they have no conflicts of interest to this work.

Acknowledgments

The authors acknowledge financial support from Natural Science Foundation of China (No.22264004, 22464004, 22074130), the Natural Science Foundation of Guangxi (2024GXNSFAA010431, 2021GXNSFAA220092), the Key Research and Development Project of Guangxi (No. AB18126048), the Guangxi Innovation-driven Development Special Fund Project (No. AA18118013-10).

Appendix A. Supplementary data

Supplementary data to this article can be found online at https://doi.org/10.1016/j.talanta.2025.127873.

Data availability

Data will be made available on request.

References

[1] Q. Li, X. Li, P. Zhou, R. Chen, R. Xiao, Y. Pang, Split aptamer regulated CRISPR/Cas12a biosensor for 17β-estradiol through a gap-enhanced Raman tags based lateral flow strategy, Biosens. Bioelectron. 215 (2022) 114548.
[2] Z. Chang, B. Zhu, J. Liu, X. Zhu, M. Xu, J. Travas-Sejdic, Electrochemical aptasensor for 17β-estradiol using disposable laser scribed graphene electrodes, Biosens. Bioelectron. 185 (2021) 113247.
[3] T. Qian, J. Bao, X. Liu, G. Oudeng, W. Ye, A "turn-on" fluorescence resonance energy transfer aptasensor based on carbon dots and gold nanoparticles for 17β-estradiol detection in sea salt, RSC Adv. 13 (40) (2023) 27772–27781.
[4] A.C. Singh, M.H. Asif, G. Bacher, B. Danielsson, M. Willander, S. Bhand, Nanoimmunosensor based on ZnO nanorods for ultrasensitive detection of 17β-Estradiol, Biosens. Bioelectron. 126 (2019) 15–22.
[5] D. Xiang, N. Li, G. Yang, H. Yu, X. Li, L. Qiu, Y. Chen, L. Liu, X. Gong, Development and validation of a liquid chromatography-tandem mass spectrometry method for the determination of polymixin B1, B2, ile-B1, E1, and E2 in human plasma and its clinical pharmacokinetic application, J. Pharmaceut. Biomed. Anal. 250 (2024) 116403.
[6] L.J. van Winden, M. Kok, M. Acda, V. Dezentje, S. Linn, R.-Z. Shi, H.H. van Rossum, Simultaneous analysis of E1 and E2 by LC-MS/MS in healthy volunteers: estimation of reference intervals and comparison with a conventional E2 immunoassay, J. Chromatogr. B 1178 (2021) 122563.
[7] B. Nuvoli, A. Sacconi, G. Bottillo, F. Sciarra, R. Libener, A. Maconi, M. Carosi, G. Piperno, E. Mastropasqua, M. Papale, E. Camera, R. Galati, DHEA-S, Androstenedione, 17-β-estradiol signature as novel biomarkers for early prediction of risk of malignant pleural mesothelioma linked to asbestos-exposure: a preliminary investigation, Biomed. Pharmacother. 175 (2024) 116662.
[8] G. Chen, W. Dai, C. Hu, H. Zang, S. Sun, S. Zhen, L. Zhan, C. Huang, Y. Li, Ratiometric electrochemiluminescence of zirconium metal–organic framework as a single luminophore for sensitive detection of HPV-16 DNA, Anal. Chem. 96 (1) (2023) 538–546.
[9] M.-H. Gao, M.-C. Pan, P. Zhang, W.-B. Liang, X. Zhong, Y. Zhuo, Identification and quantification of 5-methylcytosine and 5-hydroxymethylcytosine on random DNA sequences by a nanoconfined electrochemiluminescence platform, Anal. Chem. 95 (25) (2023) 9598–9604.
[10] Z. Li, J. Cheng, L. Huang, W. Li, Y. Zhao, W. Lin, Aging diagnostic probe for Research on aging and evaluation of anti-aging drug efficacy, Anal. Chem. 93 (41) (2021) 13800–13806.
[11] H. Chi, L. Wang, S. Wang, G. Liu, An electrochemiluminescence sensor based on CsPbBr3 -zquantum dots and poly (3-thiophene acetic acid) cross-linked nanogold imprinted layer for the determination of benzo(a)pyrene in edible oils, Food Chem. 426 (2023) 136508.
[12] M.P. Abuçafy, A.S. Mori, B.L. Caetano, S.J.L. Ribeiro, L.A. Chiavacci, Cyclodextrin-metal-organic framework (CD-MOF)/organic-inorganic hybrid composite as a potential material for drug delivery devices, J. Mol. Struct. 1314 (2024) 138717.
[13] X. Gao, X. Ren, Y. Ai, M. Li, B. Zhang, G. Zou, Luminophore-surface-engineering-enabled low-triggering-potential and coreactant-free electrochemiluminescence for protein determination, Anal. Chem. 95 (17) (2023) 6948–6954.
[14] R. Yuan, Q. Liu, H. Hong, H. Ma, L. Xiao, Y. Li, D. Jiang, N. Hao, K. Wang, Enhanced cathodic electrochemiluminescent microcystin-LR aptasensor based on surface plasmon resonance of Bi nanoparticles, J. Hazard Mater. 434 (2022) 128877.
[15] J. Li, M. Xi, L. Hu, H. Sun, C. Zhu, W. Gu, A controlled release aptasensor utilizing AIE-active MOFs as high-efficiency ECL nanoprobe for the sensitive detection of adenosine triphosphate, Anal. Chem. 96 (5) (2024) 2100–2106.
[16] L. Zheng, Q. Li, X. Deng, Q. Guo, D. Liu, G. Nie, A novel electrochemiluminescence biosensor based on $Ru(bpy)_3^{2+}$-functionalized MOF composites and cycle amplification technology of DNAzyme walker for ultrasensitive detection of kanamycin, J. Colloid Interface Sci. 659 (2024) 859–867.
[17] S. Zhu, X. Lin, P. Ran, Q. Xia, C. Yang, J. Ma, Y. Fu, A novel luminescence-functionalized metal-organic framework nanoflowers electrochemiluminesence sensor via "on-off" system, Biosens. Bioelectron. 91 (2017) 436–440.
[18] M. Liang, Y. Gao, X. Sun, R.-M. Kong, L. Xia, F. Qu, Metal-organic framework-based ratiometric point-of-care testing for quantitative visual detection of nitrite, J. Hazard Mater. 469 (2024) 134021.
[19] H. Peng, T. Romero, V. Papaefthimiou, P. Bertani, V. Ritleng, $[Ru(bpy)_3]^{2+}$-functionalized polydopamine-coated polyurethane foam as an easily reusable macroscopic heterogeneous catalyst for visible-light photocatalysis, Mol. Catal. 545 (2023) 113183.
[20] Y. Yang, H. Jiang, J. Li, J. Zhang, S.-Z. Gao, M.-L. Lu, X.-Y. Zhang, W. Liang, X. Zou, R. Yuan, D.-R. Xiao, Highly stable Ru-complex-based metal-covalent organic frameworks as novel type of electrochemiluminescence emitters for ultrasensitive biosensing, Mater. Horiz. 10 (8) (2023) 3005–3013.
[21] J. Li, C. Chen, F. Luo, Z. Lin, J. Wang, A. Huang, Y. Sun, B. Qiu, Highly sensitive biosensor for specific miRNA detection based on cascade signal amplification and magnetic electrochemiluminescence nanoparticles, Anal. Chim. Acta 1288 (2024) 342123.
[22] J. Yang, Y. Zhao, L. Qian, Y. Yu, Y. Zhang, J. Zhang, Modularization of dual recognized CRISPR/Cas12a system for the detection of Staphylococcus aureus assisted by hydrazone chemistry, J. Hazard Mater. 476 (2024) 134877.
[23] Q. Wang, Z. Zhang, L. Zhang, Y. Liu, L. Xie, S. Ge, J. Yu, Photoswitchable CRISPR/Cas12a-Amplified and Co3O4@Au nanoemitter based triple-amplified diagnostic electrochemiluminescence biosensor for detection of miRNA-141, ACS Appl. Mater. Interfaces 14 (29) (2022) 32960–32969.
[24] C. Tan, G. Xie, S. Wu, C. Song, J. Zhang, X. Yi, J. Wang, H. Tang, Simultaneous detection of breast cancer biomarkers circROBO1 and BRCA1 based on a CRISPR-Cas13a/Cas12a system, Biosens. Bioelectron. 258 (2024) 116373.
[25] J. Yuan, L. Wang, L. Huang, K. He, H. Wang, X. Xu, B. Su, J. Wang, CRISPR–Cas12a-Mediated hue-recognition lateral flow assay for point-of-need detection of Salmonella, Anal. Chem. 96 (1) (2023) 220–228.
[26] Y. Yang, J. Yang, F. Gong, P. Zuo, Z. Tan, J. Li, C. Xie, X. Ji, W. Li, Z. He, Combining CRISPR/Cas12a with isothermal exponential amplification as an ultrasensitive sensing platform for microRNA detection, Sensor. Actuator. B Chem. 367 (2022) 132158.
[27] S.B. Seo, J. Lee, E. Kim, J. Lim, S. Jang, S.U. Son, Y. Jeong, T. Kang, J. Jung, K. G. Lee, S.-W. Lee, K. Kim, E.-K. Lim, On-site detection of methicillin-resistant Staphylococcus aureus (MRSA) utilizing G-quadruplex based isothermal exponential amplification reaction (GQ-EXPAR), Talanta 275 (2024) 126073.
[28] W. Bai, A. Cui, M. Liu, X. Qiao, Y. Li, T. Wang, Signal-off electrogenerated chemiluminescence biosensing platform based on the quenching effect between ferrocene and $Ru(bpy)_3^{2+}$-Functionalized metal–organic frameworks for the detection of methylated RNA, Anal. Chem. 91 (18) (2019) 11840–11847.
[29] W. Zhang, T. Przybycien, J.M. Breuer, E. von Lieres, Solving crystallization/precipitation population balance models in CADET, Part II: size-based Smoluchowski coagulation and fragmentation equations in batch and continuous modes, Comput. Chem. Eng. 192 (2025) 108860.
[30] Y. Zhang, L. Xie, S. Feng, F. Liu, Y. Luo, Mechanistic study on the nanocomplexation between curcumin and protein hydrolysates from Great Northern bean (Phaseolus vulgaris L.) for delivery applications in functional foods, Lwt 139 (2021) 110572.
[31] J. Lu, C. Li, Y. Guo, Y. Feng, Y. Song, R. Li, L. Tian, J. Wang, Solid-state $Ru(bpy)_3^{2+}$ electrochemiluminescence sensor for trace detection of fenpropathrin using loofah sponge-like carbon nanofibers and CdS, Microchim. Acta 191 (10) (2024) 570.

[32] A.C. Singh, M.H. Asif, G. Bacher, B. Danielsson, M. Willander, S. Bhand, Nanoimmunosensor based on ZnO nanorods for ultrasensitive detection of 17β-Estradiol, Biosens. Bioelectron. 126 (2019) 15–22.
[33] Y. Liu, B. Li, Y. Yao, B. Yang, T. Tian, Y. Miao, B. Liu, An electrochemiluminescence sensor for 17β-estradiol detection based on resonance energy transfer in α-FeOOH@CdS/Ag NCs, Talanta 221 (2021) 121479.
[34] T. Yan, T. Wu, S. Wei, H. Wang, M. Sun, L. Yan, Q. Wei, H. Ju, Photoelectrochemical competitive immunosensor for 17β-estradiol detection based on ZnIn2S4@NH2-MIL-125(Ti) amplified by PDA NS/Mn:ZnCdS, Biosens. Bioelectron. 148 (2020) 111739.
[35] R. Manzoor, A. Sehrish, H. Wang, R. Xiang, Y. Li, D. Wu, Q. Wei, Competitive ECL immunosensor for ultrasensitive 17β-estradiol detection based on synergistic promotion strategy using CdSe–ZnSe nanocomposites, Talanta 267 (2024) 125160.
[36] Y. Wang, X. Zhao, M. Zhang, X. Sun, J. Bai, Y. Peng, S. Li, D. Han, S. Ren, J. Wang, T. Han, Y. Gao, B. Ning, Z. Gao, A fluorescent amplification strategy for high-sensitive detection of 17 β-estradiol based on EXPAR and HCR, Anal. Chim. Acta 1116 (2020) 1–8.
[37] Y. Jiang, Y. Song, J. Yu, C. Tong, Electrochemical detection platform based on graphene-zinc oxide composite nanomaterials for 17β-estradiol determination in milk, Alex. Eng. J. 100 (2024) 170–175.
[38] Y. Xia, Y. Liu, Y. Tang, Y. Chen, T. Li, F. Zhao, B. Zeng, A liposome encapsulated methylene blue-mediated electrochemical and UV–visible dual mode split-type immunoassay for the detection of 17β-estradiol, Talanta 276 (2024) 126243.